

Combating Interference for Long Range LoRa Sensing

Binbin Xie

University of Massachusetts Amherst
binbinxie@cs.umass.edu

Jie Xiong

University of Massachusetts Amherst
jxiong@cs.umass.edu

ABSTRACT

Wireless sensing has become a hot research topic recently, enabling a large range of applications. However, due to the intrinsic nature of employing weak target-reflection signal for sensing, the sensing range is limited. Another issue is the strong interference from surroundings and therefore a lot of wireless sensing systems assume there is no interferer in the environment. One recent work explored the possibility of employing LoRa signal for long range sensing which is a favorable step in addressing the first issue. However, the interference issue becomes even more severe with LoRa due to its larger sensing range. In this paper, we propose *Sen-fence* – a LoRa-based sensing system – to significantly increase the sensing range and at the same time mitigate the interference. With careful signal processing, *Sen-fence* is able to maximize the movement-induced signal variation in software to increase the sensing range. To address the interference issue, we propose the concept of “virtual fence” to constrain sensing only within the area of interest. The location and size of virtual fence can be flexibly controlled in software to meet the requirements of different applications. *Sen-fence* is able to (i) achieve a 50 m sensing range for fine-grained human respiration, which is twice the state-of-the-art; and (ii) efficiently mitigate the interference to make LoRa sensing work in practice.

CCS CONCEPTS

• **Human-centered computing** → *Ubiquitous and mobile computing systems and tools*.

KEYWORDS

LoRa Sensing, Interference, Virtual Fence, Long Sensing Range

ACM Reference Format:

Binbin Xie and Jie Xiong. 2020. Combating Interference for Long Range LoRa Sensing. In *The 18th ACM Conference on Embedded Networked Sensor Systems (SenSys '20)*, November 16–19, 2020, Virtual Event, Japan. ACM, New York, NY, USA, 13 pages. <https://doi.org/10.1145/3384419.3430731>

1 INTRODUCTION

Wireless sensing has attracted a lot of research attention recently with a variety of wireless signals being employed for sensing including Wi-Fi [40, 42, 47], RFID [29, 32, 41], 60 GHz [39], acoustic [22, 28, 36] and visible light [17, 18]. The rationale behind wireless

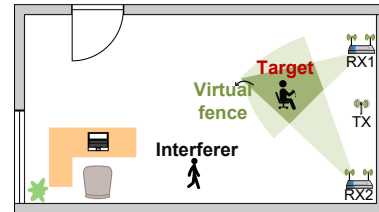


Figure 1: An example scenario for virtual fence.

sensing is that wireless signals get reflected from the target and the reflection signals vary with target movements. By analyzing the signal variation, rich target information can be obtained. The unique advantage of wireless sensing is that the target does not need to be equipped with any sensor(s), and the wireless signal itself is utilized to sense the target. A large range of applications have been enabled by wireless sensing including localization [33], tracking [7, 42], gesture/activity recognition [37, 49] and vital sign monitoring [24].

However, due to the intrinsic nature of employing weak reflection signals for sensing, the sensing range is much smaller than the communication range. Take Wi-Fi as an example. The communication range of Wi-Fi can be up to tens of meters but the state-of-the-art sensing range for Wi-Fi is just eight meters [47]. The sensing range for acoustic and 60 GHz signals are even smaller [36, 39]. Therefore, long range sensing is a major challenge for wireless sensing, and we believe many applications (e.g., disaster survivor search) would benefit if long range sensing becomes possible.

Fortunately, LoRa [19, 25, 26] technology designed for low-power and long range communication among IoT devices was recently standardized. Owing to the chirp design and forward error correction [19], the communication range of LoRa signals can be a few kilometers in the rural area, which is orders of magnitude higher than that of Wi-Fi and acoustic signals. LoRa thus presents a great potential in increasing the range of wireless sensing. In the latest work [48], the authors demonstrated the feasibility of increasing the sensing range to around 25 m using LoRa signal, which is a significant improvement. However, while LoRa does bring in a much longer sensing range, the interference issue becomes even more severe. Interference is a well-known issue [30, 44] for contact-free wireless sensing and reliable sensing performance usually can only be achieved in an environment with little or even no interference. For short range systems such as acoustic-based sensing, it is reasonable to sometimes ignore the interference issue because the sensing range is small and thus the interference range is also small. For Wi-Fi based sensing, interference is already a serious problem [38, 46]. We observe that the interference in LoRa is much more severe than that in Wi-Fi. For LoRa, an interferer even 15 m away from the target still interferes. Therefore, although the sensing range is increased, the interference range of LoRa is also much larger and if not properly addressed, LoRa sensing cannot work well in practice.

Permission to make digital or hard copies of all or part of this work for personal or classroom use is granted without fee provided that copies are not made or distributed for profit or commercial advantage and that copies bear this notice and the full citation on the first page. Copyrights for components of this work owned by others than ACM must be honored. Abstracting with credit is permitted. To copy otherwise, or republish, to post on servers or to redistribute to lists, requires prior specific permission and/or a fee. Request permissions from permissions@acm.org.

SenSys '20, November 16–19, 2020, Virtual Event, Japan

© 2020 Association for Computing Machinery.

ACM ISBN 978-1-4503-7590-0/20/11...\$15.00

<https://doi.org/10.1145/3384419.3430731>

The state-of-the-art approach dealing with interference in sensing is to separate the target-reflection signal from the interference signal [7, 8, 42] mixed at the receiver. However, this approach requires a large antenna array for signal separation in spatial domain [15, 27, 34] or a large channel bandwidth for signal separation in time domain [7, 8]. Unfortunately, LoRa does not have either of them. The channel bandwidth for LoRa is just 0.5 MHz which is much smaller than that of millimeter wave and even Wi-Fi. Also, there are usually only two antennas equipped at a LoRa gateway [48]. Some other systems [21, 43] propose to convert signals into the frequency domain and apply filters to remove the interference. This method works well when the target and interferer have dramatically different motion frequencies. For many real-life scenarios, the target and interferer have overlapping motion frequencies and this method does not work well.

In this paper, we propose *Sen-fence* and introduce the concept of *virtual fence* to mitigate the interference issue in wireless sensing as shown in Figure 1. Specifically, we create a *virtual fence* to constrain sensing only within the area of interest. As long as the interferer is outside of the virtual fence, the effect of interference can be greatly mitigated. The basic idea of wireless sensing is that the target-reflection signals vary with target movement. The sensing performance is closely related to the amount of signal variation. The larger the signal variation, the better the sensing performance.

The key idea of realizing this *virtual fence* is to increase the movement-induced signal variation to its maximum possible value if the reflection signal is from inside the *virtual fence* and keep the signal variation unchanged if the movement occurs outside of the virtual fence. With just one receiver, the wireless sensing can be constrained within a beam area (i.e., beam virtual fence). Note that the proposed method is completely different from traditional beamforming scheme. To create a beam radiation pattern using beamforming, an antenna array is required [11, 35]. However, with our proposed method, one antenna suffices to create a beam virtual fence. In this work, because we do not require the transmitter and receiver to be time-synchronized, the phase readings at the receiver vary randomly [47, 48]. Thus a second antenna is employed to obtain stable phase difference readings for sensing, rather than serving the antenna array function in beamforming. With two receivers, the sensing area can be further constrained as a “spot” virtual fence. The size of the “spot” fence can be purely controlled in software to adapt to different requirements. For example, if a person in a chair is the sensing target, we can create a virtual fence of 0.8 m \times 0.8 m to cover the chair. If a queen-size bed is the area of interest, we can create a virtual fence of 2 m \times 2 m to cover the bed.

So the key question here is how to only maximize the movement-induced signal variation in a defined region (i.e., within the virtual fence). In this work, we mathematically model signal propagation and reflection to quantify the relationship between target movements and the corresponding signal variations. Note that both signal amplitude and phase vary during the process of target movements and thus both can be utilized for sensing. In this work, we employ the phase variation for sensing because lots of hardware can report more accurate phase readings [10, 34]. A larger movement-induced phase variation indicates a better sensing performance. When the phase variation is very small, it can easily be buried in noise without being detected. We analyze the factors affecting the sensing performance

and propose a novel signal processing scheme to maximize the phase variation purely in software to improve the sensing performance. As phase variation is maximized, the sensing range is significantly increased. What is more important is that we can confine this phase variation maximization within the virtual fence to mitigate the effect of interference. To summarize, this paper makes the following contributions:

- We present a LoRa-based contact-free sensing system that is capable of achieving long range sensing. *Sen-fence* achieves a sensing range of 50 meters, twice the state-of-the-art sensing range for fine-grained respiration monitoring. The strong penetration capability of LoRa enables accurate respiration sensing even through 5 concrete walls at a distance of 9.3 m.
- We propose the concept of virtual fence to mitigate the severe interference in wireless sensing. We analyze the factors affecting the sensing performance and propose a novel signal processing method to maximize the signal variation only if the signal is reflected from the area of interest.
- The proposed method is verified with both theoretical analysis and experiments. We design, implement, and evaluate the performance of *Sen-fence* with two example applications: fine-grained respiration sensing and coarse-grained gesture tracking. Comprehensive evaluations demonstrate the effectiveness of our proposed method in mitigating the interference and increasing the sensing range. We believe the proposed method can be applied to benefit other sensing applications and be applied to other wireless signals for sensing.

2 PRELIMINARIES

In this section, we introduce the basics of LoRa, and how to employ two antennas to obtain stable phase difference readings for sensing.

2.1 LoRa basics

LoRa is one of the most popular low-power wide-area network (LP-WAN) technologies projected to support connections among billions of IoT devices [19]. LoRa offers a long communication range and a strong penetration capability through obstacles, making it a promising candidate for long range wireless sensing [9]. The key reason for this long range is the Chirp Spread Spectrum (CSS) modulation design which enables LoRa to detect weak signals even 20 dB below the noise floor [19]. As a result, compared to other wireless technologies such as Wi-Fi, LoRa signals is also able to achieve a larger sensing range [48]. However, a larger sensing range also means LoRa sensing is more likely to be affected by interference.

2.2 Obtaining stable phase difference

In LoRa systems, the transmitter and receiver are not synchronized so there is a small difference between the carrier frequencies of the transmitter and receiver which is termed as carrier frequency offset (CFO). The small difference can be tolerated and is not a problem for communication [19]. However, it causes severe issues when we employ the raw phase readings for sensing. Because of CFO, the phase readings retrieved from the receiver randomly jump between 0 and 2π , and thus cannot be utilized for sensing. Fortunately, LoRa gateways are typically equipped with two antennas [48] and they

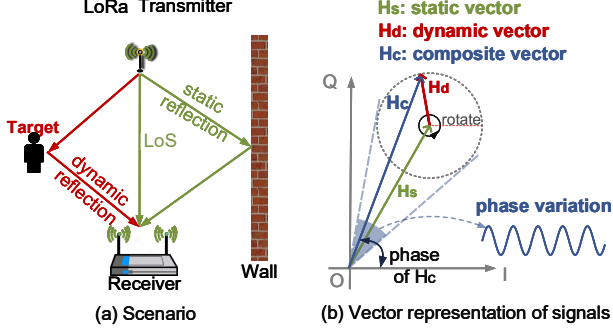


Figure 2: Signal paths for human sensing.

share the same oscillator and thus have the same random phase offset. Although the raw phase from one antenna randomly jumps, the phase difference between two antennas is stable and thus can be utilized for sensing.

3 SYSTEM DESIGN

In this section, we introduce the signal propagation model for LoRa sensing followed by the design of virtual fence. We then propose to maximize the target-induced phase variation, and confine the phase-maximization within the virtual fence.

3.1 Employing LoRa Signal for Sensing

Let us consider a simple example scenario in Figure 2(a), where there exists one target and a wall in the environment. The signal received at the receiver is composed of not just the signal reflected from the target but also the signal reflected from the wall and the line-of-sight (LoS) signal. The signal paths can thus be grouped into two categories: static path and dynamic path. The dynamic path is the target movement induced signal path and the static path consists of the LoS path and the reflection path from the static wall.

All the signals can be represented in the vector space as shown in Figure 2(b), where the composite signal vector is the vector sum of the dynamic signal vector¹ and static signal vector [24]. Note that vector representation is widely used to model the relationship between the signal variation and human movement [24, 31, 37]. During the target movement process, the static path signal does not change and the dynamic path signal varies. The phase of a signal vector is defined as the angle between the vector and I-axis, and the length of the signal vector is its amplitude. The amplitude of the dynamic vector can be considered as a constant² for a small movement such as respiration. On the other hand, the phase of dynamic vector varies significantly. A chest displacement of 0.5 cm causes a phase change of 11° ($\frac{2\pi \times 0.5\text{cm}}{33\text{cm}} \times 360^\circ$) for 915 MHz LoRa signal. Thus, during the movement process, the dynamic signal vector rotates with respect to the static signal vector in the vector space, leading to the phase variation of the composite signal vector as shown in Figure 2(b). This composite signal is what we retrieve from the receiver and the phase variation of the composite signal is used for sensing. When we employ the phase variation for sensing, the sensing performance is quantitatively related to the amount of

¹We use *dynamic signal vector* and *dynamic vector* interchangeably in this paper.

²The amplitude of dynamic vector is related to the distance between the target and sensing devices. Compared with meter-level target-device distance, a chest displacement of 0.5 cm during respiration causes less than 1% signal amplitude change.

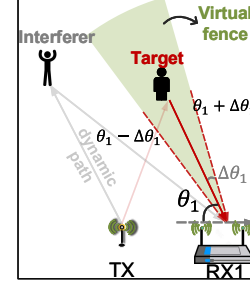


Figure 3: Virtual fence generated by one receiver.

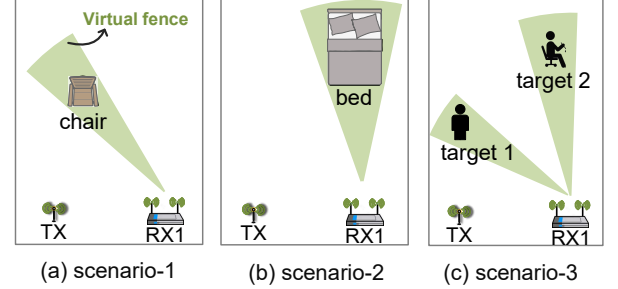


Figure 4: Examples of virtual fence with one receiver.

phase variation. A larger phase variation indicates a clearer signal variation pattern and thus a better sensing performance.

3.2 Creating Virtual Fence for Sensing

In this section, we introduce how to create a virtual fence to confine sensing within an area of interest. The location and size of the virtual fence can be controlled in software. We first explain how to form a beam-shaped virtual fence using one receiver, and then introduce how to construct a spot-shaped virtual fence with two receivers.

Virtual fence formed by one receiver. As shown in Figure 3, the virtual fence formed by one receiver is a beam-shaped area originated from the receiver. Different from beamforming which requires many antennas to create a thin beam, *Sen-fence* is able to create an arbitrarily thin beam-shaped virtual fence with just two antennas.³ If the target is located at the direction of θ_1 with respect to the receiver, then a virtual fence in the range of $[\theta_1 - \Delta\theta_1, \theta_1 + \Delta\theta_1]$ will be created. Note that we need to know area of interest before we can determine the values of θ_1 and $\Delta\theta_1$. For instance, if we would like to monitor the respiration of a static target in the chair, we can adjust the value of θ_1 to the direction of chair, and adopt a small $\Delta\theta_1$ to form a thin fence to cover the chair as shown in Figure 4 (a). If we would like to monitor the sleeping process of a target, we configure the beam direction θ_1 towards the bed, and employ a larger $\Delta\theta_1$ to cover the bed as shown in Figure 4 (b). If there are two targets, two virtual fences can be created to cover each of them as shown in Figure 4 (c).

Virtual fence formed by two receivers. With just one receiver, we are able to confine the sensing in a beam region. However, if the interferer and the target are at the same direction with respect to the receiver RX1 as shown in Figure 5, then the “beam” virtual fence is not able to mitigate the interference from the interferer. To cope with the problem, we propose to employ a second receiver to form

³The second antenna is used to cancel out the random phase offset.

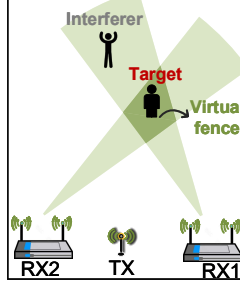


Figure 5: “Spot” virtual fence formed by two receivers.

a spot-shaped virtual fence. Similar to the first receiver $RX1$, the second receiver $RX2$ can form a second beam virtual fence which is in the range of $[\theta_2 - \Delta\theta_2, \theta_2 + \Delta\theta_2]$ with respect to $RX2$. The overlapping region of the two beam virtual fences is a spot. We can control the size of this spot virtual fence in software to adapt to different application requirements. The idea is to only maximize the signal variation in the overlapping region, which is presented in Section 3.3 and 3.4.

3.3 Maximizing Signal Phase Variation

In this section, we propose our method to maximize the movement-induced phase variation for a better sensing performance. We first theoretically analyze the factors affecting the signal phase variation, and then propose a signal processing method to maximize the phase variation. Maximizing the phase variation does not only mitigate the interference but also increases the sensing range, which is validated in Section 4.3.

3.3.1 Factors affecting the sensing performance. As mentioned in the previous section, a larger signal phase variation indicates a better sensing performance. Without loss of generality, we take human respiration sensing as the example to illustrate the concept. As shown in Figure 6, the inhalation and exhalation of human chest during the process of respiration cause the dynamic signal path to vary and accordingly the composite signal to vary.

Phase difference between the static and dynamic vectors. We pick three near-by target locations with a same distance from the sensing hardware. We can observe that for the same amount of chest displacement, the induced phase variations at the three locations are dramatically different as shown in Figure 6. While the smallest phase variation is observed at Location 1, a much larger phase variation is obtained at Location 3. From this experiment, we know that besides the target-device distance, the target location also greatly affects the sensing performance. Two nearby locations separated by just a few centimeters can present dramatically different sensing performance. We next explain why the location affects the sensing performance.

As described in Section 3.1, during the process of respiration, the dynamic vector rotates with respect to the static vector. For the same amount of chest displacement, the amount of phase rotation is the same. Although the amount of phase rotation of the dynamic vector is the same, different target locations lead to different start positions of the phase rotation in the vector space. In Figure 7, we show the respiration-induced phase variations when the dynamic vector starts rotation from three different positions corresponding to three different target locations. We can see that the induced phase variations of the composite vector are very different. Through careful analysis, we

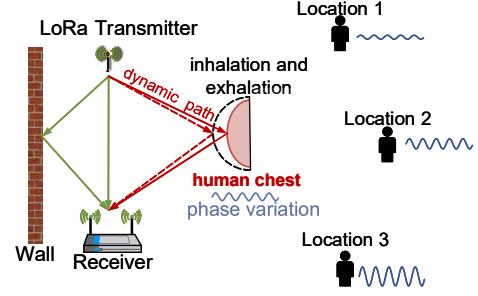


Figure 6: Respiration patterns vary with the target locations.

find that *the phase difference between the static vector and dynamic vector* is a key factor affecting the amount of phase variation induced. Specifically, when the phase difference between the dynamic vector and static vector is 180° (Figure 7(c)), the respiration-induced phase variation is the largest. Therefore, we can tune the phase difference to be 180° for a better sensing performance. For small movements such as respiration, the phase rotation of the dynamic vector during the process is small. We can thus use the average phase of the dynamic vector to calculate the phase difference.

Amplitude of composite vector. We further discover that besides the phase difference, the amplitude of the composite vector also affects the phase variation. By tuning the amplitude of the composite vector, we can further increase the movement-induced phase variation. As shown in Figure 8, we keep the phase difference between the dynamic and static vectors as 180° and reduce the amplitude of the composite vector. We can clearly see that the induced phase variation is further increased.

We now present the theoretical analysis of tuning the amplitude of the composite signal for a larger phase variation. As shown in Figure 8(a), the phase difference between the dynamic and static vectors is kept as 180° , and $|H_d|$, $|H_c|$ and $|H_s|$ form a triangle. By applying the trigonometric function [5], we obtain $\frac{|H_d|}{\sin(0.5\Delta\phi_c)} = \frac{|H_c|}{\sin(0.5\Delta\phi_d)}$, where $\Delta\phi_d$ is the phase rotation of the dynamic vector, and $\Delta\phi_c$ is the induced phase variation of the composite vector. Thus, the target-induced phase variation $\Delta\phi_c$ can be represented as:

$$\Delta\phi_c = 2 \times \arcsin \frac{|H_d| \cdot \sin(0.5\Delta\phi_d)}{|H_c|}. \quad (1)$$

From Equation (1), we can observe that by tuning the three parameters $\Delta\phi_d$, $|H_d|$ and $|H_c|$, we can enlarge the induced phase variation $\Delta\phi_c$. Among the three parameters, $\Delta\phi_d$ is determined by the target movement which is out of our control. The amplitude of the dynamic vector $|H_d|$ is determined by the distance between the target and the LoRa sensing devices. Moving the target to change the target-device distance can tune the value of $|H_d|$ but is intrusive and requires the target to be involved. Thus, among the three parameters, only the amplitude of composite vector $|H_c|$ is left for us to tune. As \arcsin in Equation (1) is a monotonically increasing function, we can decrease the value of $|H_c|$ to achieve a larger phase variation ($\Delta\phi_c$). While $|H_d|$ is a constant, the minimum value of $|H_c|$ is reached when $|H_c|$ is perpendicular to $|H_s|$ as shown in Figure 8(c). The target-induced phase variation ($\Delta\phi_c$) is now maximized to π .

In summary, by simultaneously (i) tuning the phase difference between the static and dynamic signal vectors to 180° and (ii) reducing the amplitude of composite signal vector to its minimal value, we

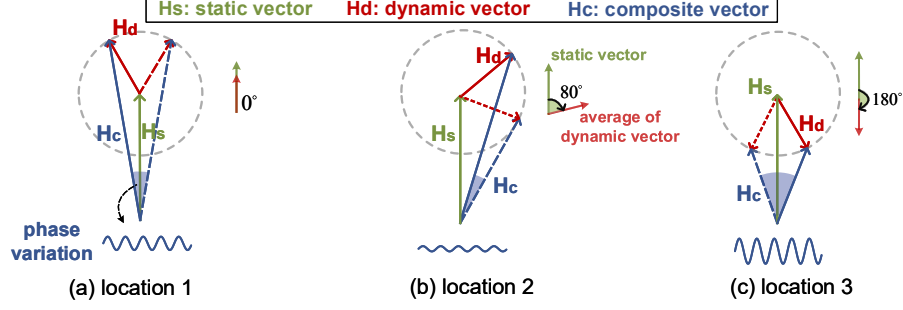


Figure 7: Different phase differences can induce different phase variations for the same target movement.

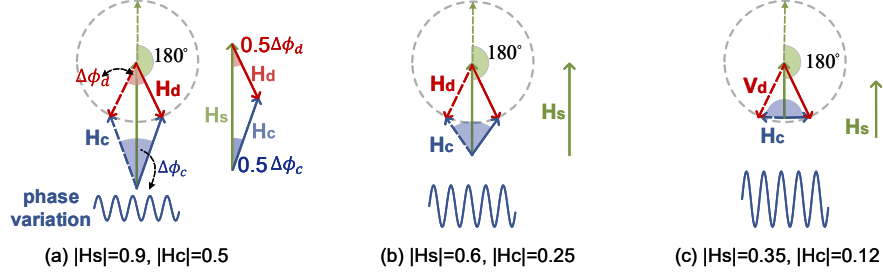


Figure 8: Decreasing the amplitude of static vector can reduce that of composite vector, accordingly induces larger phase variation.

can maximize the movement-induced phase variation to achieve a better sensing performance.

3.3.2 Maximizing movement-induced phase variation. In this section, we present the detailed steps for tuning these two factors analyzed above to maximize the target-induced phase variation. While the dynamic signal vector is decided by the target movement and out of our control, we can change the static vector to achieve the 180° phase difference between the static and dynamic vectors. Moreover, the amplitude of the composite signal vector can also be changed by tuning the static vector. Thus, we propose to tune the static signal vector to meet the two requirements.

The static signal vector is composed of LoS signal and reflections from static objects such as the wall. To change the static signal vector, the straightforward solution is to move the transceiver pair, the static reflector, or include a new static reflector. However, physically moving the reflector (or transceiver pair) is not just intrusive but also difficult to control in practice. We may need to move the reflector multiple times before achieving a satisfying sensing performance, which is time-consuming.

To tune the static signal purely in software without requiring moving or adding any objects, we propose a signal processing method. We demonstrate that adding a signal vector in software can serve the same role as physically adding a reflector in our benchmark experiment (Section 4.2). As shown in Figure 9(a), in the vector space, originally the phase difference between the static vector and dynamic vector is not 180° and the induced phase variation is small. After we add a static signal H_m to the original signal H_s as shown in Figure 9(b), the new static vector H_{snew} now has a phase difference of 180° with respect to the dynamic vector H_d , and the amplitude of the composite vector H_c is also minimized. Now the amount of induced phase variation is maximized to π .

Deriving the Added Signal. So how to obtain the added signal H_m to maximize the phase variation in software? If the dynamic vector is known, we can calculate H_m based on the vector relationship

described in the previous section. The challenging part is that the dynamic vector is unknown and we only have the composite vector H_c which is the received signal at the receiver. Therefore, we propose a joint search scheme to search the phase ϕ_m and amplitude $|H_m|$ of the added signal H_m simultaneously. For a given pair of phase ϕ_m and amplitude $|H_m|$, the added signal is $H_m = |H_m|e^{-j\phi_m}$.

- **Phase value (ϕ_m).** We search ϕ_m in the range of 0 to 2π at a step size of $\Delta\phi$.
- **Signal amplitude ($|H_m|$).** To search the optimal value of $|H_m|$, we need to know the search range. From Figure 9(b), vectors H_s , H_m and H_{snew} form a triangle. Thus, $|H_m| < |H_s| + |H_{snew}|$. From Figure 9(b), we also know that $|H_{snew}| < |H_d|$. The amplitude of the dynamic signal $|H_d|$ is usually much smaller than the static signal $|H_s|$, we can thus obtain the following relationship to restrict our search range: $|H_m| < 2|H_s|$. The background static vector H_s can be measured when there is no target. We therefore search in $[0, 2|H_s|]$ at a step size of $\Delta|H|$.

There is a trade-off between the computational cost and sensing performance. The proposed search has a computational complexity of $O(N^2)$. From our empirical results, a step size of $\frac{\pi}{180}$ for phase search and a step size of $0.1|H_s|$ for the amplitude search work well and the average time cost for search is still small (0.1 s). The impact of step size is studied in our evaluation part.

Adding Signal in Software. After obtaining the created signal $H_m = |H_m|e^{-j\phi_m}$, we add it to the original received signal (H_c). As discussed before, the original composite signal H_c is the sum of the dynamic signal H_d and original static signal H_s . For a time interval with N signal samples $H_c = (H_{d1} + H_s, H_{d2} + H_s, \dots, H_{dN} + H_s)$, the new signal samples after adding the created signal H_m is:

$$\begin{aligned} H_{cnew} &= (H_{d1} + H_s + H_m, H_{d2} + H_s + H_m, \dots, H_{dN} + H_s + H_m) \\ &= (H_{d1} + H_{snew}, H_{d2} + H_{snew}, \dots, H_{dN} + H_{snew}) \end{aligned}$$

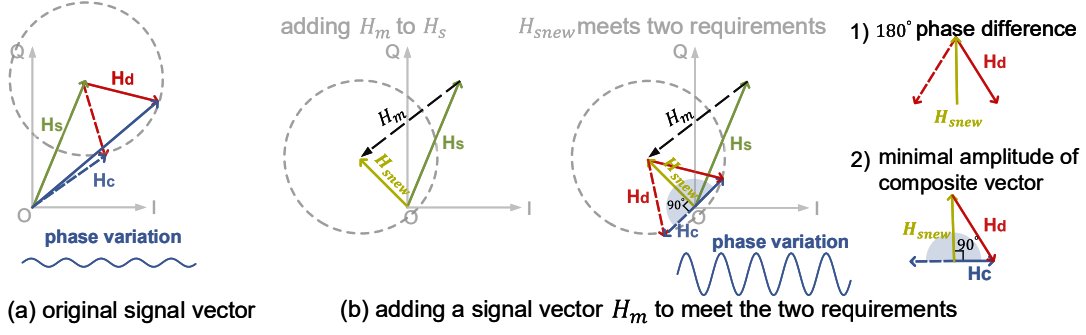


Figure 9: Effect of adding a signal vector in software.

where the phase of H_{cnew} is the new target-induced phase after H_m is added. During the joint search process, each amplitude-phase combination leads to one H_m . We add each H_m to the original signal in software, and obtain one new target-induced phase variation. Among these new phase variations, we pick the maximum one and accordingly obtain the optimal pair of ϕ_m and $|H_m|$.

3.4 Confining Phase Variation Maximization Within Virtual Fence

In this section, we introduce the proposed method to confine phase variation maximization within the defined virtual fence.

3.4.1 “Beam” virtual fence with one receiver. Given the target directions θ_1 as shown in Figure 3, we aim to form a “beam” virtual fence in the range of $[\theta_1 - \Delta\theta_1, \theta_1 + \Delta\theta_1]$ and only maximize the movement-induced phase variation in the virtual fence. To achieve this, instead of searching the added signal vector H_m in the full range as described in Section 3.3.2, we only search a smaller range based on the target direction θ_1 and beam width $\Delta\theta_1$.

Step 1: Deriving H_m using new static vector H_{snew} . As shown in Figure 9(b), the new static vector H_{snew} is the sum of the original static vector H_s and the added signal vector H_m . Based on this vector relationship, we can derive:

$$H_m = H_{snew} - H_s \quad (2)$$

Since the static vector H_s can be measured when there is no target, if we can obtain H_{snew} , we are able to calculate H_m . We next describe how to obtain H_{snew} .

Step 2: Obtaining the phase of H_{snew} using target direction. Now we explain the relationship between the target direction θ_1 and the phase value of the new static signal H_{snew} . Once this relationship is established, given the range of target direction $[\theta_1 - \Delta\theta_1, \theta_1 + \Delta\theta_1]$, we can obtain the corresponding phase values of H_{snew} . From Figure 3, we know that the target direction θ_1 is related to the phase difference $\Delta\phi$ between the signals received at the two antennas as:

$$\Delta\phi = \frac{2\pi\Delta d \cdot \cos\theta_1}{\lambda} \quad (3)$$

where Δd is the spacing between the two antennas. Note that in this work, we employ the phase difference between two antennas to obtain the stable phase information for sensing. Thus, the phase (ϕ_d) of the dynamic vector H_d is actually calculated as the phase difference ($\Delta\phi$) of the dynamic signals received at the two antennas. Therefore, we can link the phase ϕ_d of the dynamic vector and the

target direction θ_1 as below:

$$\phi_d = \frac{2\pi\Delta d \cdot \cos\theta_1}{\lambda} \quad (4)$$

As discussed in previous section, a phase difference of 180° between the dynamic vector and the new static vector is required to maximize the target-induced phase variation. Therefore, we can express the phase ϕ_{snew} of the new static vector using the target direction θ_1 :

$$\phi_{snew} = \frac{2\pi d \cdot \cos\theta_1}{\lambda} + \pi \quad (5)$$

Given the target direction in the range of $[\theta_1 - \Delta\theta_1, \theta_1 + \Delta\theta_1]$, the corresponding phase range of H_{snew} can be obtained. We thus do not need to search the full range $(0-2\pi)$ but a range calculated from the beam width.

Step 3: Searching the amplitude of H_{snew} . There is no relationship between the amplitude of H_{snew} and the target direction θ_1 . However, as shown in Figure 9(b), when the target-induced phase variation is maximized, $|H_{snew}| < |H_s|$. Therefore, we search the amplitude $|H_{snew}|$ in the range $[0, |H_s|]$. The step size is set as $0.1|H_s|$ and $|H_s|$ can be measured when there is no target.

We now jointly search ϕ_{snew} and $|H_{snew}|$ in the ranges described in Step 2 and 3. Each pair of ϕ_{snew} and $|H_{snew}|$ can lead to one vector signal H_{snew} , and accordingly one H_m . By adding each H_m to the original signal, a phase variation can be derived. Among these phase variations, we pick the maximum one and obtain the corresponding H_m . The obtained H_m is the vector we need to add to maximize the movement-induced phase variation for the target inside the beam virtual fence. Note that the added signal vector H_m changes with the original static vector. Therefore, if the environment gets changed, the original static vector H_s also changes, and accordingly a new tuning process in software is required.

3.4.2 Employing a second receiver to create a spot virtual fence. For most scenarios, a beam-shape virtual fence is enough to mitigate the interference issue. However, it is still possible that the target and the interferer are located at the same direction with respect to the receiver as shown in Figure 5. In this challenging scenario, the virtual fence created by RX1 still covers both target and interferer.

We now explain how to include a second receiver to address this issue. Similar to the first receiver RX1, the second receiver RX2 can also form a beam-shaped virtual fence to cover the target. While the interferer severely interferes with the target at RX1, the interference at RX2 is much smaller. Therefore, with two receivers, one interferer can only severely interfere target sensing at both receivers when the interferer is located within the spot virtual fence.

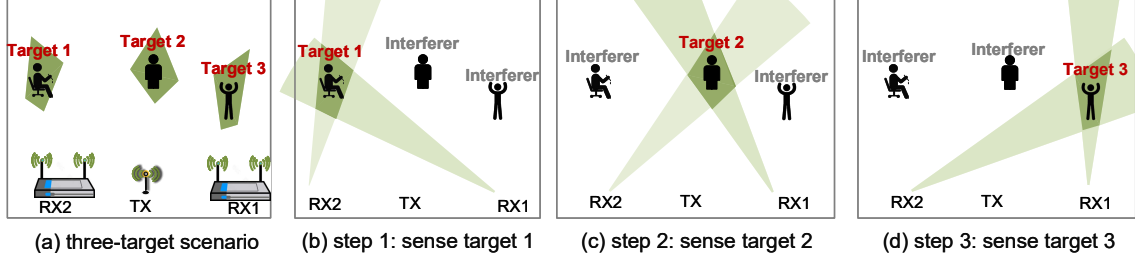


Figure 10: One example for multi-target sensing with virtual fence.

3.4.3 Multi-target sensing. The proposed concept can be applied to enable multi-target sensing which is a well-known challenge in wireless sensing. When there are multiple targets, we can create multiple “spot” virtual fences with two receivers to cover each of the targets and sense them one by one. Consider a simple example shown in Figure 10(a) with three spot virtual fences corresponding to three targets. We first sense target 1 while considering target 2 and 3 as interferers (Figure 10(b)). Then, when target 2 is sensed, target 1 and 3 are considered as interferers (Figure 10(c)). Similarly, target 3 can be sensed (Figure 10(d)).

4 EVALUATION

We conduct comprehensive experiments to evaluate the performance of *Sen-fence*. In Section 4.1, we introduce the hardware used. In Section 4.2, we present the benchmark experiments to verify each component of our design. In Section 4.3 and 4.4, we evaluate the end-to-end performance of *Sen-fence* using two application examples.

4.1 Hardware

The experiment setup involving one LoRa transmitter and two LoRa receivers is shown in Figure 12(a). The LoRa transmitter [4] is composed of an Arduino Uno working as the processing unit together with a commodity Semtech SX1276 module working as the radio front-end. The LoRa signals are transmitted at a carrier frequency of 915 MHz. The transmission range of LoRa signal is determined by three parameters [19]: the spreading factor (SF), channel bandwidth (BW), and coding rate (CR). We configure SF = 12, BW = 125 KHz, and CR = 4/8 [19] in our design. The receiver is implemented on USRP X310 [6] equipped with two antennas. The sampling rate of the receiver is set as 500 KHz. A Thinkpad X1 Extreme laptop with the 8th Generation Intel Core i7-8850H processor is connected to the two receivers via a switch and Ethernet cables to collect signal samples for data processing. We employ directional antennas with an 8 dBi gain [48] at both the transmitter and receivers. We use Labview [3] to retrieve data samples from USRP.

4.2 Benchmark Experiments

We start with two benchmark experiments to validate the effectiveness of our proposed scheme. For all the experiments in this part, we employ fine-grained respiration sensing as the application example to illustrate the concept.

4.2.1 Maximizing the target-induced phase variation. We first evaluate the effectiveness of *Sen-fence* in maximizing the target-induced phase variation. The experiment is conducted in a corridor as shown in Figure 16. The distance between the LoRa transmitter

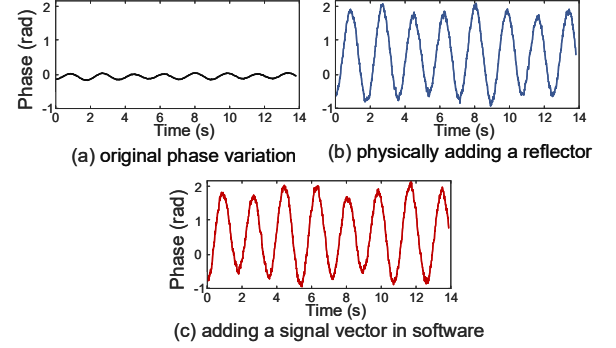


Figure 11: Verifying tuning the static signal.

and receiver is set as 1 m. All the antennas are placed at a height of 1.05 m above the ground to better capture the target’s chest movement. The target sits 10 m away from the LoRa transceivers.

Tuning the static vector using a physical reflector. As described in Section 3.3.1, to maximize the movement-induced phase variation, we need to tune the static signal to meet two requirements, i.e., a phase difference of 180° between the static and dynamic vectors, and a minimal amplitude of the composite vector. To verify the effectiveness of tuning the static signal, we first tune the static signal using a physical reflector (i.e., a $1.5 \text{ m} \times 1.5 \text{ m}$ metal plate) to create a reflection signal which is added to the original static signal. We move the metal reflector towards the receiver at a step size of 1 cm and measure the magnitude of the phase variation at each step. We stop until we achieve a phase variation larger than $\frac{5}{6}\pi$.⁴ After tens of attempts, we achieve a phase variation larger than $\frac{5}{6}\pi$ for respiration as shown in Figure 11(b), which is much larger than the original phase variation (0.06π) in Figure 11(a). This result demonstrates the effectiveness of employing a physical reflector to tune the static signal to maximize the movement-induced phase variation. During the process of this experiment, we adjust the location of the metal plate many times before we achieve the targeted sensing performance. Thus, physically tuning the static reflector is effective but time-consuming and inconvenient in practice.

Tuning the static signal vector in software. In this experiment, instead of physically tuning the static vector as described above, we create a signal vector in software and add it to the original received signal. Following the method presented in Section 3.3.2, we jointly search the phase and amplitude of the added signal H_m to obtain the optimal values contributing to the maximal movement-induced phase variation. To maintain a low computational cost, we employ a

⁴Theoretically, the achievable maximal phase variation is π . However, this is difficult to achieve in reality. Thus, we stop when the phase variation is larger than $\frac{5}{6}\pi$.

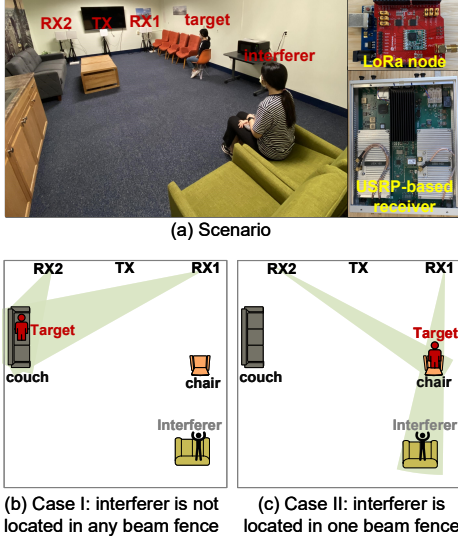


Figure 12: Verifying the effect of virtual fence.

step size of $\frac{\pi}{180}$ for phase search in the range of $[0, 2\pi]$ and a step size of $0.1|H_s|$ for amplitude search in the range of $[0, 2|H_s|]$. The search process takes around 0.1 s to complete. The maximal phase variation is shown in Figure 11(c), where the achieved respiration-induced phase variation is much larger and clearer than the original one (Figure 11(a)). Comparing Figure 11(b) and (c), we can see that injecting a static vector purely in software can achieve a similar effect as using a physical reflector.

We further evaluate the impact of step sizes on the performance. We first keep the step size for amplitude search unchanged (i.e., $0.1|H_s|$), and vary the step size for phase search from $\frac{\pi}{360}$ to $\frac{\pi}{180}$, $\frac{\pi}{90}$ and $\frac{\pi}{45}$. The corresponding amplitudes of the induced phase variations are 0.93π , 0.85π , 0.77π , and 0.59π , respectively. Then, we keep the step size for phase search unchanged (i.e., $\frac{\pi}{180}$), and vary the step size for amplitude search from $0.05|H_s|$ to $0.2|H_s|$ and $0.3|H_s|$. The corresponding amplitudes of the induced phase variations are 0.89π , 0.80π , and 0.73π , respectively. From these results, we can see that a smaller step size does bring in better performance. Therefore, there is a trade-off between the computational cost (search time) and the sensing performance. To maintain a good balance between search time and performance, we employ $\frac{\pi}{180}$ as the step size for phase search, and $0.1|H_s|$ for amplitude search in our experiments.

4.2.2 Confining sensing in a virtual fence. We conduct this experiment in a lounge room with a size of $4.5 \text{ m} \times 7.7 \text{ m}$ as shown in Figure 12(a). The distances between the transmitter and each receiver are 1.5 m and 1.8 m, respectively. We ask one volunteer to act as the target and the other to serve as the interferer. Both of them breathe naturally and the ground-truth respiration rates are 35 rpm (respiration per minute) and 21 rpm, respectively. The ground-truth respiration pattern and rate are obtained using HEXOSKIN Smart Garments [2]. We compute the respiration rate using the Fast Fourier Transform (FFT) [21] for comparison and evaluation.

Verify the effectiveness of virtual fence. We form two virtual fences of different sizes at a couch and a chair respectively, as shown in Figure 12(b) and (c). In Figure 12(b), the beam direction and width are $\theta_1 = 34^\circ$, $\Delta\theta_1 = 7.5^\circ$ for RX1 and $\theta_2 = 59^\circ$, $\Delta\theta_2 = 11^\circ$ for RX2.

For Figure 12(c), the beam parameters are $\theta_1 = 79^\circ$, $\Delta\theta_1 = 6.5^\circ$, $\theta_2 = 146^\circ$, and $\Delta\theta_2 = 5^\circ$. We demonstrate the effectiveness of our virtual fence design using two cases below.

Case I: We create a virtual fence at the couch as shown in Figure 12(b), where the interferer is not located within either beam virtual fence of the two receivers. During the respiration process, the reflection signals from the target and from the interferer get mixed at the receivers. As shown in Figure 13(a), without our proposed method, the obtained phase variations from both RX1 and RX2 are quite small. Also because of the interference, the respiration patterns are corrupted. The respiration rate errors are 1.1 rpm and 1.4 rpm, respectively. After applying the proposed virtual-fence method in Figure 13(b), the obtained phase variations at RX1 and RX2 are much larger. The interference is mitigated and we can observe clear periodical respiration patterns. The respiration rate errors are decreased to 0.2 rpm (i.e., a reduction of 81.8%) and 0.25 rpm (i.e., a reduction of 82.1%), respectively at the two receives. These results illustrate the effectiveness of applying the virtual fence to confine sensing within the area of interest to mitigate the interference.

Case II: We now create a virtual fence to cover the chair as shown in Figure 12(c), where the interferer is located at the same direction as the target with respect to RX1. In this case, even we apply the proposed virtual fence scheme at RX1, we are not able to recover the clean respiration pattern for the target. Therefore, we employ the second receiver RX2 to recover the clean respiration pattern because the interferer is not located in the beam virtual fence of RX2. As presented in Figure 14(a), without the proposed method, the original phase variations at RX1 and RX2 do not show clear periodical patterns and the variations are very small. With the proposed virtual fence, we can obtain a clean respiration pattern at RX2 as shown in Figure 14(b) and the respiration rate error is just 0.2 rpm. These results are consistent with our analysis in Section 3.4.

To evaluate the impact of size of the virtual fence, we use two pairs of beam widths for RX1 and RX2: the first pair is larger ($\Delta\theta_1 = 10^\circ$, $\Delta\theta_2 = 7.5^\circ$) than what we originally use in Figure 12(c), and the second pair is smaller ($\Delta\theta_1 = 2.5^\circ$, $\Delta\theta_2 = 2.5^\circ$). For the first pair, the maximized phase variation at RX2 for respiration is roughly the same as that in Figure 14(b). However, for the second pair, the maximized phase variation at RX2 decreases. This is because the smaller beam widths cannot fully cover the target and then the obtained phase variation is not maximized.

Note that the beam width is purely controlled in software. We can flexibly set it a large value for a large area of interest and a small value for a small area. Theoretically, we can achieve below 0.1° precision on the USRP platform and this precision is mainly determined by the resolution of the signal readings retrieved from the USRP. We can narrow down the beam width to cover smaller non-human targets. As shown in Figure 15, to sense the vibration of a $9 \text{ cm} \times 8 \text{ cm}$ generator which is 3 m away from the LoRa transceivers, we can set the beam width as 4° . To track an even smaller robot of a size of $5.5 \text{ cm} \times 9 \text{ cm}$, we can employ a beam width of 3° to cover it.

4.3 Respiration sensing

Human respiration sensing is an important application in health monitoring and elderly care. Contactlessly monitoring respiration is

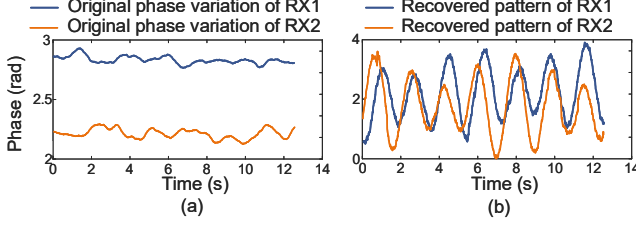


Figure 13: Verifying the virtual fence design for Case I.

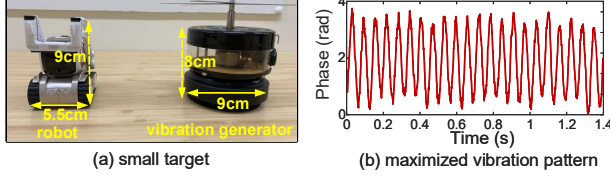


Figure 15: Narrow beam sizes for smaller targets.

particularly important during a pandemic like COVID-19 because contact-free approaches could provide a safer means to continuously monitor respiratory behaviors for patients as well as for clinicians. In the disaster survivor search, long range respiration sensing can be applied to detect survivors buried deep in the debris. In this section, we show several scenarios which can be challenging for other wireless signals but are possible with *Sen-fence*.

Long range sensing. We conduct experiments in a corridor with a length of 65 m as shown in Figure 16 to evaluate the sensing range with our proposed method. We increase the distance between the human target and the LoRa transceivers from 15 m gradually to 60 m. The sensed respiration patterns with and without the proposed method are presented in Figure 18. We can see that when the distance is 15 m, the obtained respiration patterns are clear even without the proposed method. This demonstrates the intrinsic larger sensing range of LoRa compared to other wireless technologies such as Wi-Fi. The current state-of-the-art Wi-Fi respiration sensing range is just 8 m [47]. However, when the distance is increased to 35 m, we can see that without the proposed method, the respiration pattern is severely corrupted. This is because the respiration-induced phase variation is so small that it can be easily buried in noise. On the other hand, with the proposed method, we can still obtain a clear respiration pattern. When we increase the distance to 50 m, our proposed method can still clearly sense the respiration. When the distance is further increased to 60 m, we find that the sensing accuracy starts decreasing. The achieved 50 m range is twice the state-of-the-art sensing range (25 m) using LoRa signals [48].

While the experiments above are conducted with a bandwidth of 125 KHz, to evaluate the impact of LoRa bandwidth on the sensing range, we increase the bandwidth to 250 KHz and 500 KHz and keep other parameters unchanged. The experiment results show that the sensing range decreases from 50 m to 43 m and 35 m, respectively. This is because with an increased bandwidth size, the same amount of power is distributed to a larger frequency range and therefore the signal-to-ratio (SNR) of the LoRa signal decreases. Accordingly, the sensing range is also reduced. Therefore, we choose a small bandwidth of 125 KHz in our experiments for a larger sensing range.

Respiration sensing through multiple walls. We now evaluate the through-wall capability of *Sen-fence* for respiration sensing. The target sits in a classroom and we place the sensing device outside

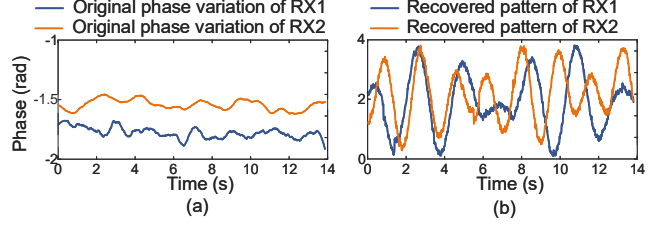


Figure 14: Verifying the virtual fence design for Case II.

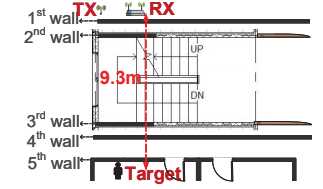
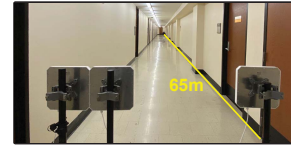


Figure 16: Corridor scenario. Figure 17: Through-wall sensing.

of the classroom with concrete walls between the target and the sensing devices. To show the penetration capability of LoRa sensing, we vary the number of concrete walls from 1 to 5. We present the setup for our 5-wall sensing in Figure 17 where the target and the sensing devices are marked on the floorplan, and the distance between them is 9.3 m. The walls are made of concrete and each wall has a thickness of around 15 cm. For each experiment, we capture the respiration pattern and calculate the absolute error of respiration rate estimation. Specifically, in all the five experiments, we can clearly obtain the respiration pattern. The corresponding errors of respiration rate estimation are 0.1 rpm, 0.15 rpm, 0.23 rpm, 0.3 rpm, and 0.4 rpm, respectively. Even in the most challenging 5-wall scenario, the achieved accuracy is still quite high. For Wi-Fi based respiration sensing, the state-of-the-art through wall capability is merely 0.5 wall [47]. We believe 5 walls is not the limit of LoRa sensing. In the current experiment environment, we are not able to find more walls for experiment. We plan to explore the limit of through-wall capability of LoRa sensing in our future work.

Long range sensing with one target and one interferer. In this part, we evaluate whether we can obtain clean respiration patterns of the target when an interferer is very close to the target. The experiment is conducted in the 65 m corridor with two receivers. The target and interferer sit in a row, and the LoRa sensing devices are deployed 20 m away from them. We decrease the distance between the target and the interferer from 2 m to 0.4 m, and evaluate whether our method can still sense the respiration of the target. When the target and the interferer are side-by-side, the distance⁵ between them is 0.4 m, which is the minimal possible distance. We observe that even when the target and interferer are side by side, *Sen-fence* is still able to obtain the target's respiration pattern accurately with a respiration estimation error of 0.4 rpm.

Through-wall sensing with multiple interferers. We now evaluate the impact of number of interferers in terms of respiration sensing accuracy. For the scenario shown in Figure 19, we create a virtual fence pointing to a chair 4.5 m away from the LoRa sensing devices with a concrete wall between the target and sensing devices. In this experiment, we vary the number of interferers from 1 to 3 to evaluate whether *Sen-fence* can work effectively. Both the target

⁵The distance is measured as the spacing between the chairs.

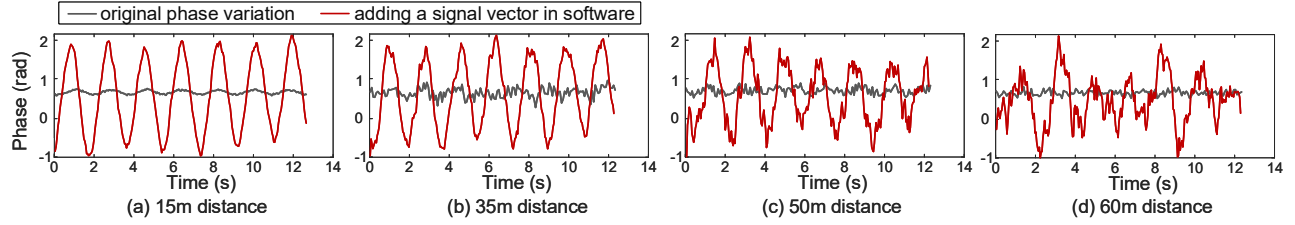


Figure 18: Detecting respiration under different distances between the target and LoRa transceivers.

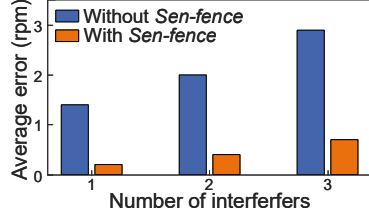


Figure 19: Through-wall respiration sensing with multiple interferers.

Figure 20: Average error of respiration rate with varying number of interferers.

Figure 21: Respiration sensing with walking interference outside the room.

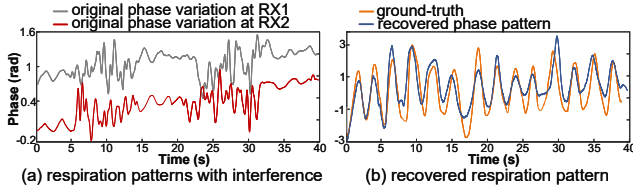


Figure 22: Respiration sensing with walking interference.

and interferers breathe naturally ranging from 18 rpm to 40 rpm. For each number of interferers, we conduct a total of 50 experiments at 2 different target locations. At each target location, we randomly vary the interferers' locations to have 25 different typologies. We present the error of the respiration rate estimation for the three cases in Figure 20. The results after mitigating the interference show that the average errors of respiration rate are 0.2 rpm, 0.4 rpm, and 0.7 rpm, for 1, 2, and 3 interferers respectively. Without the processed method, the error can be as large as 2.7 rpm.

We also evaluate the locations of three interferers in two challenging scenarios: (a) multiple interferers are located in one virtual fence beam, and (b) both two beams have interferers located inside. For the first scenario, *Sen-fence* achieves a low error of 0.5 rpm for respiration rate estimation. However, for the second scenario, the error is increased to 2.1 rpm. This is because when the interferers are located in one of the beams, we can use the second beam to accurately estimate the target's respiration. However, if multiple interferers are located in both two beams, there is no clean beam fence and therefore the error significantly increases.

Respiration sensing with interferer walking around. The human motion during walking is much larger than the chest displacement for respiration. Therefore, it is challenging to sense human respiration when the interferer walks around. We ask one volunteer to walk in the corridor outside the room to serve as the interferer while the target sits in a chair inside the room as shown in Figure 21. We present the phase variation without our proposed method in Figure 22(a). We can see the respiration pattern is severely distorted by the interferer and we are not able to obtain the target's respiration information at all. Figure 22(b) shows the phase variation pattern

with the proposed method. We can observe clear phase variation corresponding to the respiration cycles. We also plot the ground-truth respiration pattern and we can see that the obtained pattern matches the ground-truth well. Note that the ground-truth "Hexoskin Smart Shirts" device does not report the phase values. For Figure 22(b), we scale the ground-truth pattern to the same phase variation range as the obtained pattern for similarity comparison.

4.4 Gesture tracking

Gesture sensing without any sensors attached to the target provides an attractive way for human-computer interaction [20]. We aim to push the sensing range from room-level to house-level for gesture tracking. In this section, we take long range and through-wall gesture tracking as one example to evaluate our proposed method. Five hand gestures are considered including push hand, wave hand, hand moves up, clap hands, and draw a circle using one hand. Before identifying the gestures, *Sen-fence* collects the clean phase variations beforehand for all gestures when there is no interferer, and store them in the database. To recognize the gesture, we employ the correlation coefficient [8] to calculate the similarity between the recovered phase variation and the stored phase variation. The one that generates the maximal similarity is determined as the type of gesture.

Gesture tracking with daily activity interference. To evaluate whether the proposed method can deal with interference for gesture tracking, we conduct experiments in an apartment as shown in Figure 23. The LoRa transmitter, receivers, and the virtual fence are marked in the figure. In this experiment, we have one target and one interferer in the apartment. The target sits in the couch and performs gestures. The target also moves to three different locations within the virtual fence to evaluate the effect of location diversity. During the sensing process, the interferer is performing the routine daily activities including taking a shower in the bathroom, cooking in the kitchen, and taking yoga exercises in the bedroom marked in blue. The walls of the apartment are made of wood and the interference is strong. We repeat experiments 50 times for each gesture. The gesture recognition results are shown in Figure 26. We can see that *Sen-fence* can successfully obtain the phase pattern for gesture

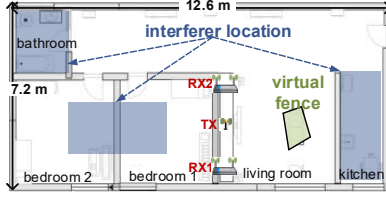


Figure 23: Gesture tracking in an apartment scenario.



Figure 24: Recovering the gesture pattern in through-wall scenario.



Figure 25: Varying the distance between the target and walking interference.

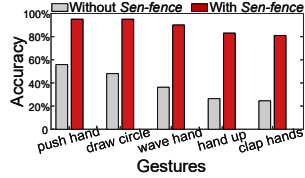


Figure 26: Gesture recognition with daily activity interference.

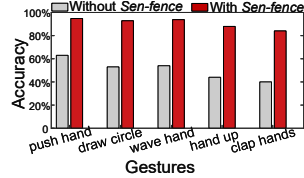


Figure 27: Gesture recognition with robot cleaner interference.

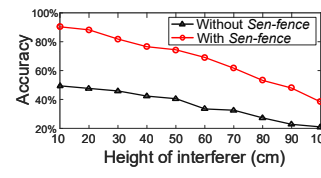


Figure 28: Impact of interference height.

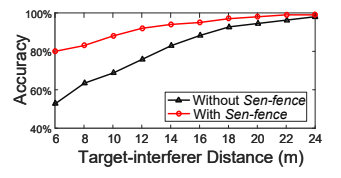


Figure 29: Impact of target-interferer distance.

recognition in a home environment where the interferer is performing daily activities. The average gesture recognition accuracy is improved from 42% to 90% with the proposed method.

Through-wall gesture tracking with a robot cleaner as the interferer. Now we conduct experiments to evaluate the sensing performance with a moving robot cleaner [1] as the interferer in the same room. The experiment setup is shown in Figure 24, where the target is sitting in a chair 8 m away from the LoRa transceivers with a wall between them, and a robot cleaner randomly moves in the same room. We make the cleaner move at its maximum speed which is 25 cm/s. The obtained gesture phase patterns are shown in Figure 30. The phase variation patterns without our proposed method are very different from the clean patterns stored in the database while the obtained phase variation patterns with our method match the clean patterns well. The gesture recognition accuracy is presented in Figure 27. With the proposed method, the average accuracy is increased from 51% to 93% with the robot cleaner moving around.

Impact of height and size of the interferer. We conduct experiments to evaluate the impact of height and size of the interferer. First, we increase the height of the robot cleaner from 10 cm to 100 cm at a step size of 10 cm by putting paper boxes on top of the robot. The LoRa devices are placed 1.05 m above the ground. The average gesture recognition accuracy is presented in Figure 28. Without *Sen-fence*, the average accuracy over all gestures is around 49% when the height of robot interferer is 10 cm. With *Sen-fence*, the average accuracy is increased to 91%. When we increase the height of the interferer, the interference becomes stronger and the corresponding recognition accuracy gradually decreases. When the height of robot is increased to 30 cm, the stronger interference makes the accuracy decrease to 43%. With *Sen-fence*, the achieved accuracy is improved to 80%. Note that when the robot height is 1 m, the interference is the strongest. In this challenging case, without applying the proposed method, the accuracy is as low as 21%. With *Sen-fence*, the accuracy is improved to around 40%. From these results, we can see that the proposed method is able to mitigate the effect of interference. However, when the interference is very strong, it can still affect the sensing performance even with the proposed method applied.

Further, we evaluate the impact of interferer size by placing four different sizes of cardboards on the robot: 5 cm × 5 cm, 10 cm ×

10 cm, 20 cm × 20 cm, and 50 cm × 50 cm. The height of robot is kept as its default value of 7 cm. The achieved recognition accuracies with *Sen-fence* are 92%, 88%, 81%, and 74% respectively. When the size of the interferer is larger, the reflection signal is stronger due to a larger reflection area and therefore a more severe interference. Also a larger cardboard also means the height of the interferer is higher and therefore stronger interference.

Impact of target-interferer distance. In this section, we conduct experiments in the corridor of a 65 m length to investigate the impact of interference on gesture sensing. As shown in Figure 25, the target performs gestures 12 m away from the LoRa sensing devices. The interferer walks around outside the virtual fence. To analyze the impact of interference, we vary the distance between the target and the interferer from 6 m to 24 m at a step size of 2 m. As shown in Figure 29, without applying the proposed method, the accuracy is below 60% when the interferer is 6 m away. When the interferer moves further away, the interference becomes weaker and the accuracies increase. We observe that even when the interferer is 16 m away from the target, interference is still significant. This result demonstrates the strong interference when employing LoRa signals for sensing and the necessity to address the interference. With the interferer closer to the target, the impact of interference becomes more severe. By applying the proposed interference mitigation method, the accuracy is significantly improved to around 80% when the interferer is 6 meters away. When the interferer is 14 m away, the achieved accuracy is 94% and the accuracy decreases to 81% without applying the proposed interference mitigation scheme. Note that in this experiment, the walking movement is much larger than the hand gesture. Therefore, even an interferer is outside the virtual fence, it can still interfere with the target. On the other hand, when the interference movement is comparable to the target movement, *Sen-fence* can effectively mitigate the effect of interference even the interferer is close by.

5 DISCUSSION

Minimizing signal variation outside of the virtual fence. *Sen-fence* only maximizes the signal variation within the virtual fence but does not minimize the signal variation outside the virtual fence. Therefore, it cannot deal with very severe interference. Maximizing the signal variation inside and minimizing the signal variation

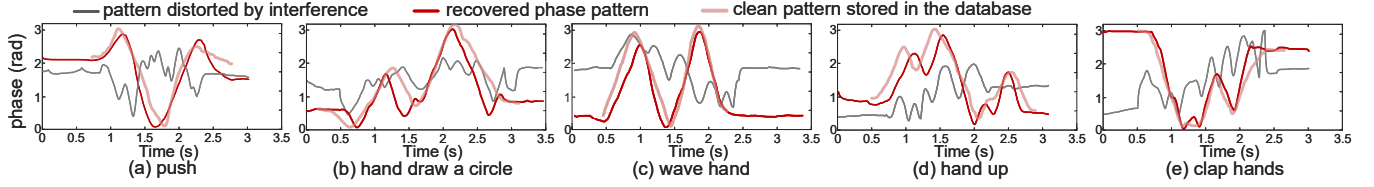


Figure 30: Recovered phase patterns for gestures.

outside the virtual fence simultaneously is a promising approach to further mitigate the impact of interference.

Locations of multiple interferers. As discussed in Section 4.3, the performance of *Sen-fence* degrades when both the two beam virtual fences have interferers located inside. This is because when we amplify the target-induced signal variation, the interference-induced signal variation will also be increased and therefore there is no clean beam fence which can be used for sensing. This is a challenging yet interesting problem for our future research.

Large activity. Interestingly, we find that the proposed system works well in tracking small movements such as respiration and gesture but not that well for large movements such as walking. This is because for a large movement, the length of the dynamic path changes tens of centimeters and even meters. This is multiple times of the wavelength and therefore the dynamic vector rotates multiple cycles. For this large phase rotation, the phase difference between the static and dynamic vectors varies from $0 \sim 2\pi$, which does not meet the requirement of a fixed difference of 180° .

Target mobility. In our experiments, the target is required to be static in the virtual fence. We believe dynamically adjusting the virtual fence to support target mobility can greatly improve the practicality of the system. To achieve this, we need to continuously track/localize the target, which leads to two challenges. First, with limited number of antennas and a small bandwidth at the LoRa gateway, angle-of-arrival based localization and time-based localization schemes do not work well. Second, when the target is moving, it is challenging to monitor the target's respiration as the target's body movements are much larger than the small chest displacement.

3D virtual fence. Currently, *Sen-fence* only considers 2D virtual fence which is in the horizontal plane because human gesture and respiration movements happen within a relatively small vertical range. It is an interesting research problem to include the vertical dimension into consideration to form a 3D virtual fence. To accomplish this, we may need a second pair of receivers deployed at different heights.

6 RELATED WORK

Our work is closely related to the research in the following domains.

LoRa-based sensing. Recently, LoRa has been used for applications including smart building [16], indoor localization [14], activity recognition [12, 13], backscatter localization and communication [23, 26]. However, these works only exploit the long range communication functionality of LoRa to collect and transfer sensor data, instead of utilizing the LoRa signal itself for contact-free sensing. In this paper, we focus on exploring LoRa signals for contact-free sensing without attaching any sensor to the target. The latest works [9, 48] move one step in this direction by employing LoRa signals for human sensing. While the main purpose of WideSee [9] is localization, they can only sense large-scale human activities such as walking and waving hands. To mitigate the strong interference,

WideSee employs a directional antenna with a beam width of 48° to point to the target area, which is still very coarse. Furthermore, without advanced signal processing, the raw sensing range is still limited and therefore a drone is utilized to carry the LoRa hardware to enable a larger coverage. The work closest to our research is [48] which employs LoRa for sensing and increases the sensing range to 25 m for human respiration sensing. However, the severe interference issue has not yet been addressed and the proposed system can only work in an ideal environment with just one target. *Sen-fence* tries to address the two fundamental issues with LoRa sensing. *Sen-fence* not only extends the sensing range of LoRa to 50 m for respiration sensing, but also effectively mitigates the interference with the virtual fence design.

Mitigating interference in contact-free sensing. An effective solution of addressing interference is to separate the signals mixed at the receiver. DeepBreath [45] separates and recovers the respiration signals for multiple targets from the received signals using a large bandwidth (1.5 GHz) and a 4-antenna array. In WiTrack2.0 [7], a large bandwidth of 1.69 GHz and 10 directional antennas are employed to separate reflection signals from different persons. Even though mD-Track [42] utilizes information from multiple dimensions for signal separation, it still employs 3 antennas and a bandwidth of 20 MHz. To conclude, the solutions for signal separation requires a large antenna array [27] and a large bandwidth [8]. However, the channel bandwidth for LoRa is just 0.5 MHz, and the LoRa gateway usually has only two antennas because LoRa is designed for low data rate and thus the main driving force of an antenna array – MIMO transmission – does not exist.

7 CONCLUSION

In this work, we present *Sen-fence*, a LoRa-based contact-free sensing system which not only enables long range sensing, but also mitigates the severe interference issue in wireless sensing. The virtual fence concept is introduced for the first time in wireless sensing to make the location and size of the sensing area under control. We propose a novel signal processing method to maximize the movement-induced signal variation. With the proposed virtual fence scheme, the interference issue is significantly mitigated. The sensing range is also increased to 50 m, twice the state-of-the-art. *Sen-fence* moves LoRa sensing one important step towards the real-life adoption. We believe the proposed methods can be applied to other wireless signals to benefit a large range of wireless sensing applications.

ACKNOWLEDGMENTS

We thank the anonymous reviewers and shepherd for their valuable comments. This work was partially supported by the UMass Amherst Institute For Applied Life Sciences Equipment Fund.

REFERENCES

- [1] DeeBot 710 robot. <https://www.ecovacs.com/global/deebot-robotic-vacuum-cleaner/deebot-710>.
- [2] Hexoskin smart garments. <https://www.hexoskin.com/>.
- [3] Labview. <https://www.ettus.com/sdr-software/labview/>.
- [4] Lora shield. <https://www.dragino.com/products/lora/item/102-lora-shield.html>.
- [5] Trigonometric function. <https://www.slideshare.net/sivapalanisamy75/trigonometry-functions>.
- [6] Usp310. <https://www.ettus.com/all-products/usp310-kit/>.
- [7] F. Adib, Z. Kabelac, and D. Katabi. Multi-person localization via rf body reflections. In *SENIX Symposium on Networked Systems Design and Implementation (USENIX NSDI)*, pages 279–292, 2015.
- [8] F. Adib, H. Mao, Z. Kabelac, D. Katabi, and R. C. Miller. Smart homes that monitor breathing and heart rate. In *Conference on Human Factors in Computing Systems (CHI)*, pages 837–846. ACM, 2015.
- [9] L. Chen, J. Xiong, X. Chen, S. I. Lee, K. Chen, D. Han, D. Fang, Z. Tang, and Z. Wang. Widesee: towards wide-area contactless wireless sensing. In *Conference on Embedded Networked Sensor Systems (SenSys)*, pages 258–270. ACM, 2019.
- [10] A. Dhekne, M. Gowda, Y. Zhao, H. Hassanieh, and R. R. Choudhury. Liquid: A wireless liquid identifier. In *International Conference on Mobile Systems, Applications, and Services (MobiSys)*, pages 442–454. ACM, 2018.
- [11] X. Fan, L. Shangguan, R. Howard, Y. Zhang, Y. Peng, J. Xiong, Y. Ma, and X.-Y. Li. Towards flexible wireless charging for medical implants using distributed antenna system. In *ACM International Conference on Mobile Computing and Networking (MobiCom)*, pages 1–15. ACM, 2020.
- [12] T. Hossain, M. A. R. Ahad, T. Tazin, and S. Inoue. Activity recognition by using lorawan sensor. In *ACM International Joint Conference and 2018 International Symposium on Pervasive and Ubiquitous Computing and Wearable Computers*, pages 58–61. ACM, 2018.
- [13] T. Hossain, Y. Doi, T. Tazin, M. A. R. Ahad, and S. Inoue. Study of lorawan technology for activity recognition. In *ACM International Joint Conference and 2018 International Symposium on Pervasive and Ubiquitous Computing and Wearable Computers*, pages 1449–1453. ACM, 2018.
- [14] B. Islam, M. T. Islam, and S. Nirjon. Feasibility of lora for indoor localization. *on-line, from semanticscholar.org*, pages 1–11, 2017.
- [15] W. Jiang, H. Xue, C. Miao, S. Wang, S. Lin, C. Tian, S. Murali, H. Hu, Z. Sun, and L. Su. Towards 3d human pose construction using wifi. In *Annual International Conference on Mobile Computing and Networking (MobiCom)*, pages 1–14. ACM, 2020.
- [16] K.-H. Ke, Q.-W. Liang, G.-J. Zeng, J.-H. Lin, and H.-C. Lee. A lora wireless mesh networking module for campus-scale monitoring: demo abstract. In *ACM/IEEE International Conference on Information Processing in Sensor Networks (IPSN)*, pages 259–260. ACM/IEEE, 2017.
- [17] T. Li, C. An, Z. Tian, A. T. Campbell, and X. Zhou. Human sensing using visible light communication. In *ACM International Conference on Mobile Computing and Networking (MobiCom)*, pages 331–344. ACM, 2015.
- [18] T. Li, Q. Liu, and X. Zhou. Practical human sensing in the light. In *International Conference on Mobile Systems, Applications, and Services (MobiSys)*, pages 71–84. ACM, 2016.
- [19] J. C. Liando, A. Gamage, A. W. Tengourti, and M. Li. Known and unknown facts of lora: Experiences from a large-scale measurement study. *ACM Transactions on Sensor Networks*, 15(2):1–35, 2019.
- [20] J. Lien, N. Gillian, M. E. Karagozler, P. Amihoud, C. Schwesig, E. Olson, H. Raja, and I. Poupyrev. Soli: Ubiquitous gesture sensing with millimeter wave radar. *ACM Transactions on Graphics*, 35(4):1–19, 2016.
- [21] J. Liu, Y. Wang, Y. Chen, J. Yang, X. Chen, and J. Cheng. Tracking vital signs during sleep leveraging off-the-shelf wifi. In *ACM International Symposium on Mobile Ad Hoc Networking and Computing (MobiHoc)*, pages 267–276. ACM, 2015.
- [22] W. Mao, M. Wang, W. Sun, L. Qiu, S. Pradhan, and Y.-C. Chen. Rnn-based room scale hand motion tracking. In *International Conference on Mobile Computing and Networking (MobiCom)*, pages 1–16. ACM, 2019.
- [23] R. Nandakumar, V. Iyer, and S. Gollakota. 3d localization for sub-centimeter sized devices. In *ACM Conference on Embedded Networked Sensor Systems (SenSys)*, pages 108–119. ACM, 2018.
- [24] K. Niu, F. Zhang, J. Xiong, X. Li, E. Yi, and D. Zhang. Boosting fine-grained activity sensing by embracing wireless multipath effects. In *International Conference on emerging Networking EXperiments and Technologies (CONEXT)*, pages 139–151. ACM, 2018.
- [25] Y. Peng, L. Shangguan, Y. Hu, Y. Qian, X. Lin, X. Chen, D. Fang, and K. Jamieson. Plora: A passive long-range data network from ambient lora transmissions. In *ACM Special Interest Group on Data Communication (SIGCOMM)*, pages 147–160. ACM, 2018.
- [26] V. Talla, M. Hesar, B. Kellogg, A. Najafi, J. R. Smith, and S. Gollakota. Lora backscatter: Enabling the vision of ubiquitous connectivity. *ACM on Interactive, Mobile, Wearable and Ubiquitous Technologies (IMWUT)*, 1(3):1–24, 2017.
- [27] D. Vasishth, A. Jain, C.-Y. Hsu, Z. Kabelac, and D. Katabi. Duet: Estimating user position and identity in smart homes using intermittent and incomplete rf-data. *ACM on Interactive, Mobile, Wearable and Ubiquitous Technologies (IMWUT)*, 2(2):1–21, 2018.
- [28] A. Wang and S. Gollakota. Millisonic: Pushing the limits of acoustic motion tracking. In *ACM conference on human factors in computing systems (CHI)*, pages 1–11. ACM, 2019.
- [29] C. Wang, L. Xie, W. Wang, Y. Chen, Y. Bu, and S. Lu. Rf-ecg: Heart rate variability assessment based on cots rfid tag array. *ACM on Interactive, Mobile, Wearable and Ubiquitous Technologies (IMWUT)*, 2(2):1–26, 2018.
- [30] F. Wang, Z. Li, and J. Han. Continuous user authentication by contactless wireless sensing. *IEEE Internet of Things Journal*, 6(5):8323–8331, 2019.
- [31] H. Wang, D. Zhang, J. Ma, Y. Wang, D. Wu, T. Gu, and B. Xie. Human respiration detection with commodity wifi devices: do user location and body orientation matter? In *ACM International Joint Conference on Pervasive and Ubiquitous Computing (UbiComp)*, pages 25–36. ACM, 2016.
- [32] J. Wang, L. Chang, S. Aggarwal, O. Abari, and S. Keshav. Soil moisture sensing with commodity rfid systems. In *International Conference on Mobile Systems, Applications, and Services (MobiSys)*, pages 273–285. ACM, 2020.
- [33] J. Wang, H. Jiang, J. Xiong, K. Jamieson, X. Chen, D. Fang, and B. Xie. Lifes: low human-effort, device-free localization with fine-grained subcarrier information. In *ACM International Conference on Mobile Computing and Networking (MobiCom)*, pages 243–256. ACM, 2016.
- [34] J. Wang, J. Xiong, H. Jiang, X. Chen, and D. Fang. D-watch: Embracing “bad” multipaths for device-free localization with cots rfid devices. *IEEE/ACM Transactions on Networking*, 25(6):3559–3572, 2017.
- [35] J. Wang, J. Zhang, R. Saha, H. Jin, and S. Kumar. Pushing the range limits of commercial passive rfids. In *SENIX Symposium on Networked Systems Design and Implementation (USENIX NSDI)*, pages 301–316, 2019.
- [36] T. Wang, D. Zhang, Y. Zheng, T. Gu, X. Zhou, and B. Dorizzi. C-fmcw based contactless respiration detection using acoustic signal. *ACM on Interactive, Mobile, Wearable and Ubiquitous Technologies (IMWUT)*, 1(4):1–20, 2018.
- [37] W. Wang, A. X. Liu, M. Shahzad, K. Ling, and S. Lu. Understanding and modeling of wifi signal based human activity recognition. In *International Conference on Mobile Computing and Networking (MobiCom)*, pages 65–76. ACM, 2015.
- [38] Y. Wang, J. Liu, Y. Chen, M. Gruteser, J. Yang, and H. Liu. E-eyes: device-free location-oriented activity identification using fine-grained wifi signatures. In *Annual International Conference on Mobile Computing and Networking (MobiCom)*, pages 617–628, 2014.
- [39] T. Wei and X. Zhang. mtrack: High-precision passive tracking using millimeter wave radars. In *International Conference on Mobile Computing and Networking (MobiCom)*, pages 117–129, 2015.
- [40] C. Wu, F. Zhang, Y. Fan, and K. R. Liu. Rf-based inertial measurement. In *ACM Special Interest Group on Data Communication (SIGCOMM)*, pages 117–129. ACM, 2019.
- [41] B. Xie, J. Xiong, X. Chen, E. Chai, L. Li, Z. Tang, and D. Fang. Tagtag: material sensing with commodity rfid. In *Conference on Embedded Networked Sensor Systems (SenSys)*, pages 338–350. ACM, 2019.
- [42] Y. Xie, J. Xiong, M. Li, and K. Jamieson. md-track: Leveraging multi-dimensionality for passive indoor wi-fi tracking. In *International Conference on Mobile Computing and Networking (MobiCom)*, pages 1–16. ACM, 2019.
- [43] P. Yang, Y. Feng, J. Xiong, Z. Chen, and X. Li. Rf-ear: Contactless multi-device vibration sensing and identification using cots rfid. In *International Conference on Computer Communications (INFOCOM)*, pages 1–10. IEEE, 2020.
- [44] Z. Yu and Z. Wang. *Human Behavior Analysis: Sensing and Understanding*. Springer, 2020.
- [45] S. Yue, H. He, H. Wang, H. Rahul, and D. Katabi. Extracting multi-person respiration from entangled rf signals. *ACM on Interactive, Mobile, Wearable and Ubiquitous Technologies (IMWUT)*, 2(2):1–22, 2018.
- [46] Y. Zeng, D. Wu, J. Xiong, J. Liu, Z. Liu, and D. Zhang. Multisense: Enabling multi-person respiration sensing with commodity wifi. *ACM on Interactive, Mobile, Wearable and Ubiquitous Technologies (IMWUT)*, 4(3):1–29, 2020.
- [47] Y. Zeng, D. Wu, J. Xiong, E. Yi, R. Gao, and D. Zhang. Farsense: Pushing the range limit of wifi-based respiration sensing with csi ratio of two antennas. *ACM on Interactive, Mobile, Wearable and Ubiquitous Technologies (IMWUT)*, 3(3):1–26, 2019.
- [48] F. Zhang, Z. Chang, K. Niu, J. Xiong, B. Jin, Q. Lv, and D. Zhang. Exploring lora for long-range through-wall sensing. *ACM on Interactive, Mobile, Wearable and Ubiquitous Technologies (IMWUT)*, 4(2):1–27, 2020.
- [49] J. Zhang, Z. Tang, M. Li, D. Fang, P. Nurmi, and Z. Wang. Crosssense: Towards cross-site and large-scale wifi sensing. In *Annual International Conference on Mobile Computing and Networking (MobiCom)*, pages 305–320. ACM, 2018.